

Calibration of LAMOST Stellar Surface Gravities Using the *Kepler* Asteroseismic Data

Liang Wang^{1,2}, Wei Wang^{1,3}, Yue Wu¹, Gang Zhao¹, Yinbi Li¹, Ali Luo¹, Chao Liu¹, Yong Zhang⁴, Yonghui Hou⁴, Yuefei Wang⁴
and
Zihuang Cao¹

[lwang;wangwei;gzhao]@nao.cas.cn

Received ; accepted

ABSTRACT

Asteroseismology is a powerful tool to precisely determine the evolutionary status and fundamental properties of stars. With the unprecedented precision and nearly continuous photometric data acquired by the NASA *Kepler* mission, parameters of more than 10^4 stars have been determined nearly consistently. However, most studies still use photometric effective temperatures (T_{eff}) and metallicities ($[\text{Fe}/\text{H}]$) as inputs, which are not sufficiently accurate as suggested by previous studies. We adopted the spectroscopic T_{eff} and $[\text{Fe}/\text{H}]$ values based on the LAMOST low-resolution spectra ($R \simeq 1,800$), and combined them with the global oscillation parameters to derive the physical parameters of a large sample of stars. Clear trends were found between $\Delta \log g$ (LAMOST – seismic) and spectroscopic T_{eff} as well as $\log g$, which may result in an over-estimation of up to 0.5 dex for the $\log g$ of giants in the LAMOST catalog. We established empirical calibration relations for the $\log g$ values of dwarfs and giants. These results can be used for determining the precise distances to these stars based on their spectroscopic parameters.

Subject headings: asteroseismology, stars: fundamental parameters, techniques: spectroscopic,

1. INTRODUCTION

Wide-field, multi-object spectroscopic surveys such as the Sloan Extension for Galactic Understanding and Exploration (SEGUE; Yanny et al. 2009), RAdial Velocity Experiment (RAVE; Steinmetz et al. 2006), and Large sky Area Multi-

Object fiber Spectroscopic Telescope (LAMOST; Cui et al. 2012), have proved to be efficient for exploring the Milky Way galaxy. Determining the fundamental parameters and chemical characteristics of a large sample of stars is particularly important and essential for better understanding the formation and structure of galaxies. Stellar surface gravity, $\log g$, is one of the most crucial parameters in stellar physics as it is closely related to the stellar luminosity and, hence, to the position of a star on the Hertzsprung-Russell Diagram (HRD). In addition, if the stellar mass is known, one can obtain the stellar radius and reddening-independent distance with precision superior to that of photometric calibrations (e.g. Breddels et al. 2010; Xue et al. 2014). On the other hand, precise determination of magnesium and calcium abundances from Mg Ib and infrared Ca II triplets in low-resolution

¹ Key Laboratory of Optical Astronomy, National Astronomical Observatories, Chinese Academy of Sciences, A20, Datun Road, Chaoyang District, Beijing 100012, China

² Max-Planck-Institut für Extraterrestrische Physik, Giessenbachstrasse, 85748 Garching, Germany

³ Chinese Academy of Sciences South America Center for Astronomy, Camino El Observatorio 1515, Las Condes, Santiago, Chile

⁴ Nanjing Institute of Astronomical Optics & Technology, National Astronomical Observatories, Chinese Academy of Sciences, Nanjing 210042, China

spectra rely heavily on the accurate determination of $\log g$ (e.g. Deeming 1960; Chmielewski 2000).

In the high-resolution ($R > 40,000$) spectroscopy, several approaches are often used for determining the $\log g$ values of cool stars. The first approach utilizes the ionization balance of neutral and singly ionized atoms of the same element, such as Fe I/II (e.g. Fuhrmann 1998; da Silva et al. 2006; Boesgaard et al. 2011). A typical $\log g$ error in this approach is 0.1-0.2 dex, which is limited by the facts that (1) the number of unblended, weak, singly ionized iron lines in stellar spectra is too small; (2) the equilibria of Fe I and Fe II are strongly affected by T_{eff} ; and (3) the non-local thermodynamic equilibrium (NLTE) effect affects the abundance of neutral iron lines by up to 0.1 dex (e.g. Mashonkina et al. 2011; Lind et al. 2012). A different method for determining $\log g$ uses the basic relation $\log g = \log M + 4 \log T_{\text{eff}} + 0.4 M_{\text{bol}}$ (e.g. Chen et al. 2000; Reddy et al. 2003; Wang et al. 2011), where the accurate absolute bolometric magnitude M_{bol} relies on the data of precise trigonometric parallaxes (e.g., acquired by the HIPPARCOS mission). A relative parallax uncertainty of 20% yields an error of 0.17 dex in $\log g$. In the HIPPARCOS CATALOGUE, $\sim 60\%$ of the stars with distances above 100 pc are characterized by a relative parallax uncertainty above 20% (van Leeuwen 2007).

Determination of stellar atmospheric parameters (T_{eff} , $\log g$, and $[\text{Fe}/\text{H}]$) from low- to medium-resolution spectra are mostly based on the spectral synthesis technique, with a library covering a wide range of T_{eff} , $\log g$, and $[\text{M}/\text{H}]$ values (e.g. Zwitter et al. 2004; Prugniel & Soubiran 2001; Sánchez-Blázquez et al. 2006; Cenarro et al. 2007). The precision associated with $\log g$ is generally lower than that obtained in high-resolution spectroscopy. For example, the error on $\log g$ determined from the SEGUE Stellar Parameter Pipeline (SSPP; Lee et al. 2008) is ~ 0.23 dex, while it is 0.5 dex for RAVE (Zwitter et al. 2008). The precision of $\log g$ for the ongoing LAMOST survey is ~ 0.2 dex for both the LAMOST stellar parameter pipeline (LASP, Wu et al. 2014; Luo et al. 2015) and LSP-3 (Xiang et al. 2015; Ren et al. 2016). Carlin et al. (2015) developed a Bayesian model to derive stellar distances from calibrated stellar spectra, and applied it to the LAMOST data. They found that the precision

with which distances could be determined was limited to 40% owing to large uncertainties associated with $\log g$. Reducing the $\log g$ uncertainty by 0.1 dex would increase the distance accuracy by $\sim 12\%$ (e.g. Liu et al. 2015).

Launched in 2009 March, the NASA *Kepler* space telescope (Borucki et al. 2010) uses a wide-field, 95-cm-aperture telescope to search for transiting Earth-sized planets in a sample of $\sim 170,000$ stars. The data collected during the first four years of the operation of this telescope not only revolutionized the extra-solar planet hunting campaign but also significantly contributed to other fields, such as asteroseismology. With the unprecedented photometric precision, researchers are, for the first time, able to precisely determine the M , R , $\log g$, and ρ values for $\sim 10^4$ stars by consistently using the asteroseismology method (e.g. Kallinger et al. 2010a; Hekker et al. 2011; Stello et al. 2013; Chaplin et al. 2014; Huber et al. 2014). These stars reveal solar-like oscillations in their power spectra, and their spectral types range from early F to late K (Chaplin et al. 2013), including both giants and dwarfs. The uncertainty associated with asteroseismic $\log g$ is typically less than 0.02 dex, which is one order of magnitude lower than the spectroscopically determined one (Hekker et al. 2013). Gai et al. (2011) showed that such asteroseismically determined $\log g$ values are almost independent of the stellar evolution model grid and contain nearly no systematic errors.

Derivation of stellar physical parameters (M , R , L) using asteroseismology scaling relations relies on T_{eff} and $[\text{Fe}/\text{H}]$ from “external” sources as inputs. The majority of asteroseismically interesting stars in the *Kepler* field (e.g. Chaplin et al. 2014) are analyzed by adopting photometric or Infra-Red Flux Method (IRFM) calibrated T_{eff} , together with Kepler Input Catalog (KIC; Brown et al. 2011) metallicities, in which systematic errors or large scatter have already been found (e.g. Dong et al. 2014). For these stars, T_{eff} and $[\text{Fe}/\text{H}]$ based on high-resolution spectroscopy remain a challenge because most of these stars are too faint for modest-sized telescopes. Recently, a significant amount of data on low-resolution ($R \sim 1,800$) spectra in the *Kepler* field have been released by the LAMOST survey (Luo et al. 2015), and a set of consistent, spectroscopic T_{eff} and $[\text{Fe}/\text{H}]$ values has been reliably determined. Therefore, it

is worthwhile to redetermine the physical parameters of these stars by replacing the photometric or KIC inputs by this new set of atmospheric parameters.

2. LAMOST SPECTROSCOPIC DATA

2.1. LAMOST Observations in the *Kepler* Field

LAMOST, also known as the “Guoshoujing Telescope,” is a reflecting Schmidt telescope with an effective aperture of ~ 4 m and a field of view (FOV) of 20 deg^2 . Four thousand fiber units in its focal plane and 16 multi-object spectrographs make it highly efficient for spectroscopic surveys. During the first three years of operation, from 2011 October, to 2014 June, LAMOST has collected over 4.1 million spectra with resolving power ($R = \lambda/\Delta\lambda$) of 1,800, and public access to these spectra has been granted in the second data release (DR2)¹. We cross-matched the DR2 and DR3 Quarter 1 (DR3Q1) catalogs with the KIC, and found 87,834 spectra of 70,703 common objects within 36 exposures in the LAMOST-*Kepler* project (De Cat et al. 2015). Atmospheric parameters for 48,486 stars out of these objects have been determined by LASP (Wu et al. 2014, 2011). The median uncertainties of T_{eff} , $\log g$, and $[\text{Fe}/\text{H}]$ were 128 K, 0.47 dex, and 0.15 dex for spectra with signal-to-noise ratios (SNRs) of ~ 50 at 477 nm, and 101 K, 0.44 dex, and 0.12 dex for spectra with SNR of ~ 100 .

2.2. LAMOST vs. High-Resolution Spectroscopy

The asteroseismic scaling relations (see Section 3.1) require T_{eff} as an input parameter. Thus, it is necessary to compare the LAMOST results with those of high-resolution spectroscopy (HRS). However, such a comparison for a large sample of stars is not always feasible, because most targets of the LAMOST observing plan are not sufficiently bright, and thus, are lacking of HR studies. Fortunately, the wealth of planet candidate hosts and other stars with noticeable values from the *Kepler* mission has generated significant interest in ground-based follow-up observations, and many of these are performed using HR spectrographs on

large telescopes, such as the 10-m-aperture Keck I telescope and the Subaru telescope. As a result, accurate stellar parameters for hundreds of FGK stars in the *Kepler* field have been determined using various techniques, providing a good opportunity to test the LAMOST low-resolution spectra parameters.

Bruntt et al. (2012, hereafter, Br2012) and Thygesen et al. (2012, hereafter, Th2012) observed 93 solar-like and 82 red giant stars using high-resolution spectrographs. They determined the $\log g$ values for these stars from global oscillation parameters, while the other atmospheric parameters T_{eff} , $[\text{Fe}/\text{H}]$, and ξ (micro-turbulent velocity) were determined using the spectroscopic method. Molenda-Żakowicz et al. (2013, hereafter, MZ2013) also analyzed 169 *Kepler* targets using spectral synthesis based on high resolution spectra collected by different ground-based telescopes. Moreover, Buchhave et al. (2012, hereafter, Bu2012) studied the HR spectra of 152 planet-host stars using Stellar Parameter Classification (SPC), which is also a realization of spectral synthesis with a grid of template spectra. To validate and characterize the planetary properties, Marcy et al. (2014, hereafter, M2014) published stellar parameters of 22 *Kepler* Objects of Interests (KOIs) using the reconnaissance spectra obtained using the HIRES spectrometer (Vogt et al. 1994). Hirano et al. (2012, 2014, hereafter, Hi2014) also derived stellar parameters for 40 KOIs using the excitation/ionization equilibrium of Fe I and Fe II lines. We divided the above samples into two groups – depending on how the values of $\log g$ were derived – using either the asteroseismology method or purely by using spectroscopic techniques.

Using the LAMOST AFGK-type star parameters catalog, we found 26, 41, 49, 39, 13, and 21 common stars with Br2012, Th2012, MZ2013, Bu2012, M2014, and Hi2014, respectively. In Figure 1, we compare the stellar parameters extracted from literature and the LAMOST catalog. The mean differences between the LAMOST and high-resolution spectroscopy parameters were $\langle \Delta T_{\text{eff}} \rangle = -1 \pm 71 \text{ K}$, $\langle \Delta \log g \rangle = 0.06 \pm 0.17 \text{ dex}$, and $\langle \Delta [\text{Fe}/\text{H}] \rangle = -0.03 \pm 0.12 \text{ dex}$ for 73 stars in the asteroseismic group (red points in Figure 1), and $\langle \Delta T_{\text{eff}} \rangle = 19 \pm 100 \text{ K}$, $\langle \Delta \log g \rangle = 0.02 \pm 0.19 \text{ dex}$, and $\langle \Delta [\text{Fe}/\text{H}] \rangle = 0.00 \pm 0.09 \text{ dex}$

¹<http://dr2.lamost.org/>

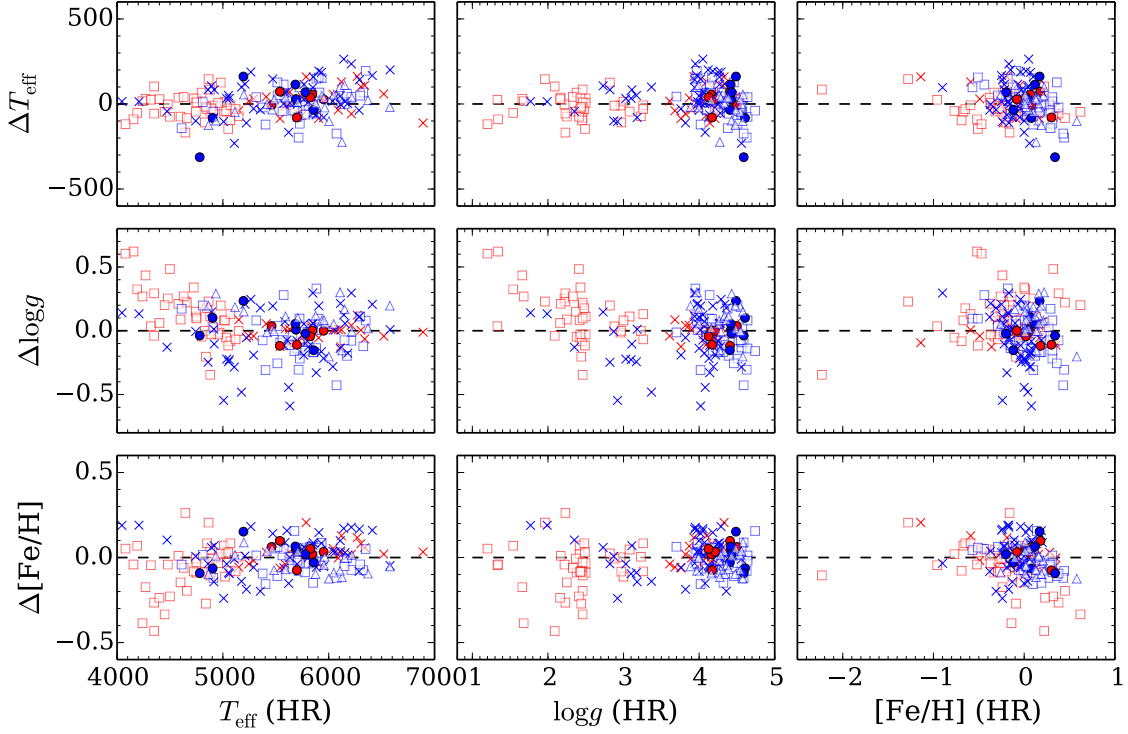


Fig. 1.— Differences between stellar parameters obtained from the LAMOST pipeline and those obtained using the HR spectroscopy, as functions of T_{eff} , $\log g$ and $[\text{Fe}/\text{H}]$, respectively. Red circles, red squares, and red crosses represent the LAMOST stars in common with M2014 (AST sub-sample), Th2012, and Br2012, respectively. All of the above adopted asteroseismic $\log g$. Blue circles, blue squares, blue crosses and blue triangles are those in common with M2014 (SME sub-sample), Bu2012, MZ2013, and Hi2014, all of which were obtained using spectral synthesis or excitation/ionization equilibrium method.

for 116 stars in the spectroscopic group (blue points in Figure 1). For all the common stars, the mean differences were $\langle \Delta T_{\text{eff}} \rangle = 11 \pm 90$ K, $\langle \Delta \log g \rangle = 0.01 \pm 0.18$ dex, and $\langle \Delta [\text{Fe}/\text{H}] \rangle = -0.01 \pm 0.10$ dex. The temperature values obtained by using the LAMOST catalog were in good agreement with those obtained from high-resolution spectra (with $\langle \Delta T_{\text{eff}} \rangle = -14 \pm 86$ K) for stars with $T_{\text{eff}} < 5,500$ K; however, the difference was slightly higher (31 ± 89 K) for hotter stars. Figure 1 also shows that $\Delta \log g$ (LAMOST – HRS) tend to increase with decreasing $\log g$ for $\log g \lesssim 2.5$, and with decreasing T_{eff} for $T_{\text{eff}} < 5,000$ K, where the HR samples were mostly from giant stars studied by Th2012, for which $\log g$ values were derived using the asteroseismology method. Th2012 presented the stellar parameters based on pure spectroscopic methods as well. In Figure 2 we plot the differences between the LAMOST $\log g$ and the asteroseismic and spectroscopic $\log g$ in Th2012, as functions of T_{eff} . It is obvious that, for both cases, the trends of $\Delta \log g$ are quite similar. Moreover, previous studies (e.g. Th2012, Takeda & Tajitsu 2015) have shown that $\log g$ obtained by the two methods are satisfactorily similar for giants. These facts suggest that LAMOST overestimated $\log g$ by up to 0.5 dex for cool giants. For metallicity, the scatter tends to increase with decreasing T_{eff} and $\log g$.

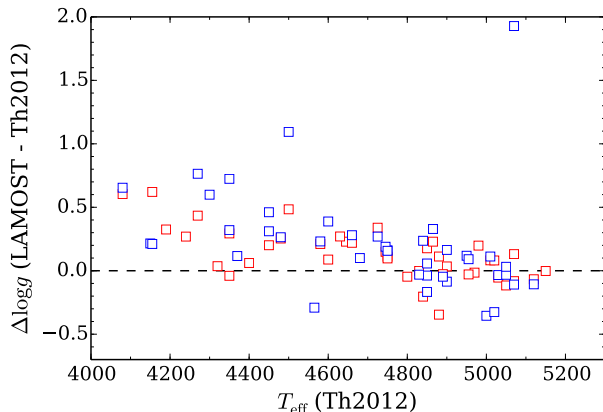


Fig. 2.— Differences between $\log g$ from the LAMOST pipeline and from Th2012, as functions of T_{eff} . Similar to Figure 1, the red and blue squares represent the parameters obtained by performing asteroseismic and spectroscopic analysis in Th2012, respectively.

3. METHOD

3.1. Asteroseismic Analysis

Solar-like oscillations are excited by the near-surface turbulent convection in a star, which is characterized by the global oscillation parameters $\Delta\nu$, corresponding to the average frequency separation between oscillation modes with consecutive radial orders n and the same spherical degree l , and ν_{max} , the frequency at which the oscillation power is maximum. The parameter $\Delta\nu$ is proportional to the square root of the mean stellar density (ρ) and is therefore given by (Ulrich 1986):

$$\Delta\nu = \sqrt{\frac{M/M_{\odot}}{(R/R_{\odot})^3}} \Delta\nu_{\odot} \quad (1)$$

with respect to the Sun. The parameter ν_{max} is assumed to be scaled with the acoustic cutoff frequency (Brown et al. 1991), and Kjeldsen & Bedding (1995) used this assumption to relate ν_{max} to the fundamental stellar parameters as follows.

$$\nu_{\text{max}} = \frac{M/M_{\odot}}{(R/R_{\odot})^2 \sqrt{T_{\text{eff}}/T_{\text{eff},\odot}}} \nu_{\text{max},\odot} \quad (2)$$

By solving Equations 1 and 2, one can obtain the relations linking the stellar mass M , radius R , mean density ρ , and surface gravity $\log g$ with the global oscillation parameters $\Delta\nu$ and ν_{max} . It is noted that $\log g$ only depends on ν_{max} for a given T_{eff} .

The values of $\Delta\nu$ and ν_{max} for different types of stars in the *Kepler* field have been used to estimate M , R , ρ and $\log g$ in various studies. For instance, Kallinger et al. (2010a) determined the parameters for $> 1,000$ red giants based on the first 138 days of the *Kepler* photometric data. Hekker et al. (2011) used the data of the first 33 days to characterize more than 10,000 giants for which solar-like oscillations have been detected. This work was later refined by Stello et al. (2013) using the *Kepler* data with a longer time baseline of 681 days. The *Kepler* mission also detected solar-like oscillations for 500 out of 2,000 pre-selected main sequence and sub-giant stars during the first 10 months of its scientific operation (Chaplin et al. 2011). The fundamental parameters of these stars were published in Chaplin et al. (2014) and led to better characterization of planets (Huber et al. 2013) and their host stars (Mathur et al. 2011; Johnson et al.

2014). Huber et al. (2014) presented the revised catalog of parameters for more than 190,000 stars for the *Kepler* Quarter 1-16 data.

Although stellar parameters can be directly derived Equations 1 and 2 as

$$\left(\frac{M}{M_\odot}\right) = \left(\frac{\nu_{\max}}{\nu_{\max,\odot}}\right)^3 \left(\frac{\Delta\nu}{\Delta\nu_\odot}\right)^{-4} \left(\frac{T_{\text{eff}}}{T_{\text{eff},\odot}}\right)^{3/2} \quad (3)$$

$$\left(\frac{R}{R_\odot}\right) = \left(\frac{\nu_{\max}}{\nu_{\max,\odot}}\right) \left(\frac{\Delta\nu}{\Delta\nu_\odot}\right)^{-2} \left(\frac{T_{\text{eff}}}{T_{\text{eff},\odot}}\right)^{1/2} \quad (4)$$

$$\left(\frac{\rho}{\rho_\odot}\right) = \left(\frac{\Delta\nu}{\Delta\nu_\odot}\right)^2 \quad (5)$$

$$\log g = \log g_\odot + \log \left(\frac{\nu_{\max}}{\nu_{\max,\odot}}\right) + \frac{1}{2} \log \left(\frac{T_{\text{eff}}}{T_{\text{eff},\odot}}\right) \quad (6)$$

$$\left(\frac{L}{L_\odot}\right) = \left(\frac{\nu_{\max}}{\nu_{\max,\odot}}\right)^2 \left(\frac{\Delta\nu}{\Delta\nu_\odot}\right)^{-4} \left(\frac{T_{\text{eff}}}{T_{\text{eff},\odot}}\right)^5 \quad (7)$$

, some sets of (M, R, T_{eff}) for a given metallicity are not permitted according to the stellar evolution theories. Grid-based methods containing a significantly large number of parameters ($M, R, T_{\text{eff}}, [\text{Fe}/\text{H}]$) returned by stellar evolution programs have been widely used to find the best match to the observed parameters (see Chaplin et al. 2013, and references therein). We adopted the Geneva stellar evolutionary tracks (Lejeune & Schaerer 2001), which cover a wide range of mass and metallicity (Z) values. The values of high-temperature opacities were taken from the OPAL data (Iglesias & Rogers 1996), and those of low-temperature opacities were taken from Kurucz (1991) or Alexander & Ferguson (1994). For stars with $M \leq 1.5M_\odot$, a core overshooting parameter of $d/H_P = 0.2$ was adopted. Mass loss of Reimers (1975) and de Jager et al. (1988) were taken into account. In previous grid-based analyses (e.g. Basu et al. 2010; Kallinger et al. 2010a; Huber et al. 2014), some widely used stellar models, such as the YREC (Yale Stellar Evolution Code; Demarque et al. 2008), DSEP (Dartmouth Stellar Evolution Program; Dotter et al. 2008), and BaSTI (Bag of Stellar Tracks and Isochrones; Pierantoni et al. 2004) models, did not account for the evolutionary stages after the helium flash. On the contrary, the evolution phases of Geneva database were calculated to the end of the early asymp-

totic giant branch (EAGB) phase for intermediate-mass stars ($2 \leq M/M_\odot \leq 5$), and to the end of the carbon burning phase for larger mass stars ($M/M_\odot \geq 7$). Therefore, the evolutionary stages following the helium flash were included for stars with $M > 2M_\odot$. As a substantial number of our samples met the above condition, we considered that our method naturally eliminates the systematic bias towards larger masses for giants in Huber et al. (2014), where post-helium flash data were not included for calculations.

To ensure that at least 10^2 models are available for the final probability density function (PDF) of each star, we generated a dense grid by interpolating the evolutionary tracks in steps of 0.02 dex for $[\text{Fe}/\text{H}]$, ranging from -2.0 to $+1.5$, and steps of $0.02 M_\odot$ for the initial mass (M_0), ranging from 0.8 to $5.0 M_\odot$. For each track, the Geneva database contained at most 51 groups of data points with T_{eff} , L , age, and M . Here, M is the stellar mass, varying with time due to the mass loss. We interpolated 500 points along the entire time span, and calculated R and $\log g$ using the basic physical relations, along with $\Delta\nu$ and ν_{\max} that were calculated according to the scaling relations in Equations 1 and 2, for each interpolated point. We adopted the solar seismic parameters $\Delta\nu_\odot = 135.1 \pm 0.1 \mu\text{Hz}$ and $\nu_{\max,\odot} = 3,090 \pm 30 \mu\text{Hz}$ that were based on the data collected by VIRGO aboard SOHO spacecraft during $\sim 11,000$ days (Huber et al. 2011). Our complete grid had a total of $\sim 1.8 \times 10^7$ points, each containing nine parameters, T_{eff} , Z , M , R , L , $\log g$, age, $\Delta\nu$, and ν_{\max} .

Stellar fundamental parameters can be subsequently derived from the observed oscillation parameters ($\Delta\nu$ and ν_{\max}) using the Bayesian approach, if T_{eff} and $[\text{Fe}/\text{H}]$ are known. The Bayes' theorem can be stated as

$$p(\boldsymbol{\theta}|\mathbf{d}, M) = \frac{p(\boldsymbol{\theta}|M)p(\mathbf{d}|\boldsymbol{\theta}, M)}{p(\mathbf{d}|M)} \quad (8)$$

, where $p(\boldsymbol{\theta}|\mathbf{d}, M)$ is the posterior probability distribution of parameters $\boldsymbol{\theta}$ for a certain model M , based on the observational data \mathbf{d} . The model M stands for an individual datum corresponding to an evolutionary status in our grid. The distribution $p(\boldsymbol{\theta}|M)$ is the prior probability distribution of $\boldsymbol{\theta}$, and the likelihood function $p(\mathbf{d}|\boldsymbol{\theta}, M)$ is the probability of obtaining \mathbf{d} , given the parameters $\boldsymbol{\theta}$

for model M . The quantity $1/p(\mathbf{d}|M)$ is the normalization term. In our case, the observational data set is $\mathbf{d} = (T_{\text{eff}}, [\text{Fe}/\text{H}], \Delta\nu, \nu_{\text{max}})$, and

$$p(\mathbf{d}|\boldsymbol{\theta}, M) = \mathcal{L}_{T_{\text{eff}}} \mathcal{L}_{[\text{Fe}/\text{H}]} \mathcal{L}_{\Delta\nu} \mathcal{L}_{\nu_{\text{max}}} \quad (9)$$

. The likelihood functions of each parameter are calculated to match the observational ones by assuming independent Gaussian-distributed errors. Therefore, we have

$$\mathcal{L}_d = \frac{1}{\sqrt{2\pi}\sigma_d} \exp \left[-\frac{(d_{\text{obs}} - d_{\text{model}})^2}{2\sigma_d^2} \right] \quad (10)$$

Some previous studies adopted uniform priors $p(\boldsymbol{\theta}|M)$ for all models in the grid (e.g. Kallinger et al. 2010a). However, it should be noted that for a star with given (M_0, Z) , the probability of its physical quantities being $(T_{\text{eff}}, R, L, \log g)$ when the star is being observed is inversely proportional to the star’s evolutionary speed in its current stage. Otherwise, the resulting stellar parameters would be biased towards the rapid evolution phases (see the description of the GOE pipeline in Chaplin et al. 2014). In our approach, the differential age of a track with a given (M_0, Z) can well represent the reciprocals of the evolutionary speeds; thus

$$p(\boldsymbol{\theta}|M_{i,j}) = C \frac{a_{i+1,j} - a_{i,j}}{a_{n,j} - a_{1,j}} \quad i = 1, 2, \dots, n-1 \quad (11)$$

, where $a_{i,j}$ is the age of the i -th interpolated point in the j -th track, C denotes the normalization factor, and $n = 500$ is the number of interpolated points along each track. In the above equation, the time span of two adjacent points $(a_{i+1,j} - a_{i,j})$ is normalized by the total time $(a_{n,j} - a_{1,j})$ of the j -th track; otherwise, the posterior probability distributions would be biased towards low-mass stars. Although larger-mass stars have shorter lifetimes than less massive stars, and hence, have lower probabilities of being observed as their higher luminosities make them visible over longer distances to a magnitude-limited survey, which, to some extent, cancels out the above age selection effect. Therefore, aim of Equation 11 only corrects the bias caused by different evolutionary speeds at different stages, rather than lifetimes, as a function of the stellar masses. In our study, uniform probabilities for stars with different (M_0, Z) were assumed, because our observed data \mathbf{d} were accurate, and the prior probabilities of (M_0, Z) were

not expected to vary significantly over such a relatively narrow parametric range.

All the sample stars in this work have been monitored by the *Kepler* space telescope with extremely high photometric precision during its scientific operation. Several research groups have devoted attention to extracting the values of $\Delta\nu$ and ν_{max} from the *Kepler* light curves using various techniques (e.g., Mosser & Appourchaux 2009; Huber et al. 2009; Kallinger et al. 2010b; Hekker et al. 2010). We employed the parameters from different literature sources, as listed in Table 1. For nonseismic parameters T_{eff} and $[\text{Fe}/\text{H}]$, we used the values returned by the LASP in the LAMOST AFGK-type star parameters catalog.

3.2. Iterative Process

In our work, the derived $\log g$ obtained using the above approach could differ from spectroscopically obtained values by as much as 0.5 dex (see Section 4.3), which could in turn yield a significant bias in T_{eff} and $[\text{Fe}/\text{H}]$. Therefore, we determined our spectroscopic parameters (T_{eff} , $[\text{Fe}/\text{H}]$ and $\log g$) iteratively. First, asteroseismic $\log g$ values (hereafter, $\log g_{\text{iter0}}$) were obtained by using the above-mentioned grid method, with T_{eff} and $[\text{Fe}/\text{H}]$ listed in the LAMOST catalog (hereafter, $T_{\text{eff,LASP}}$ and $[\text{Fe}/\text{H}]_{\text{LASP}}$), and oscillation parameters $\Delta\nu$ and ν_{max} . Then, the LAMOST spectra for all the sample stars were reanalyzed by LASP with fixed $\log g_{\text{iter0}}$, to acquire new $T_{\text{eff,iter1}}$ and $[\text{Fe}/\text{H}]_{\text{iter1}}$ values, which were then used for calculating asteroseismic $\log g_{\text{iter1}}$. We found that, in our sample, a change of +0.1 dex in $\log g$ resulted in $\Delta T_{\text{eff}} \sim +27$ K and $\Delta[\text{Fe}/\text{H}] \sim +0.02$ dex for giants, and in $\Delta T_{\text{eff}} \sim +36$ K and $\Delta[\text{Fe}/\text{H}] \sim +0.01$ dex for dwarfs. The differences between $\log g_{\text{iter1}}$ and $\log g_{\text{iter0}}$ were within ± 0.03 dex for 99% of our giants, and ± 0.01 dex for all of our dwarfs, except for only one star. These small changes in $\log g$ after the first iteration had negligible effects on T_{eff} and $[\text{Fe}/\text{H}]$ compared with the observational uncertainties because, according to Equation 6, asteroseismic $\log g$ only depends weakly on T_{eff} . Consequently, our results regarding atmospheric parameters converged after one iteration.

Table 1: Sources of oscillation parameters ($\Delta\nu$ and ν_{\max}) for stars analyzed in this work. Methods for obtaining the seismic data are described by [Kallinger et al. 2010b](#) (CAN), [Hekker et al. 2010](#) (OCT), [Mosser & Appourchaux 2009](#) (COR), and [Huber et al. 2009](#) (SYD).

Reference	Type of stars	Timespan	Method	N_{total}	N_{adopt}
Kallinger et al. (2010a)	red giants and clump stars	~ 1200 days (Q1 \sim Q13)	CAN	> 1000	630
Hekker et al. (2011)	red giants and clump stars	33 days	OCT	$> 10^4$	1548
Mathur et al. (2011)	two solar-type stars	8 months	–	2	1
Mosser et al. (2012)	red giants and clump stars	690 days (Q1 \sim Q8)	COR	218	10
Huber et al. (2013)	planet-candidate host stars	~ 1000 days (Q1 \sim Q11)	SYD	77	27
Stello et al. (2013)	red giants and clump stars	681 days (Q0 \sim Q8)	SYD	~ 13000	630
Chaplin et al. (2014)	main-sequence and sub-giant stars	~ 300 days	SYD	518	214
				Total	3060

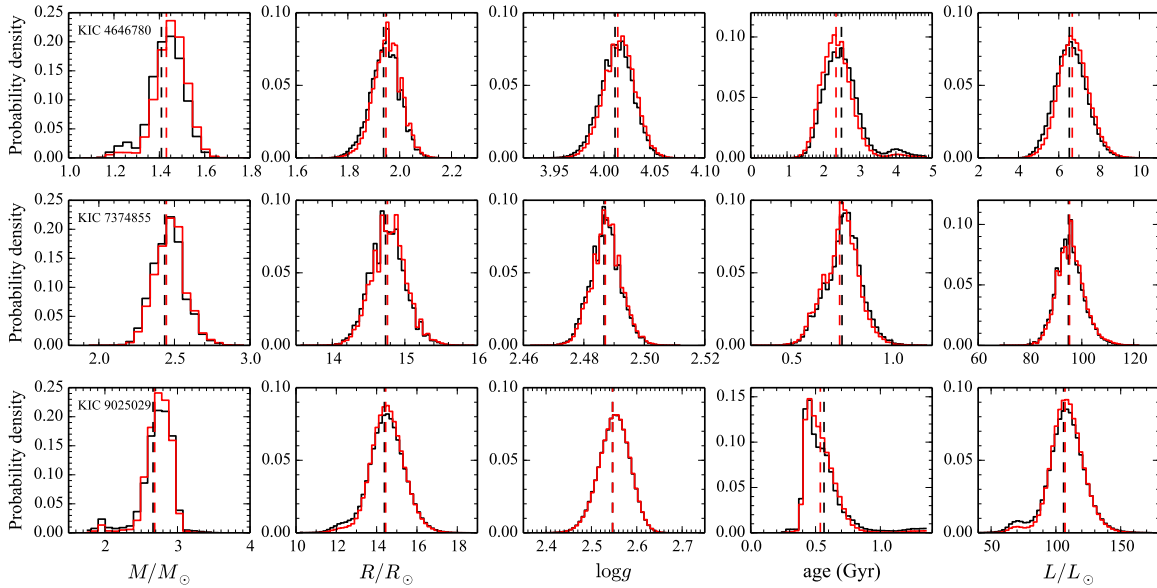


Fig. 3.— Examples of normalized PDFs of stellar parameters, for one dwarf (KIC 4646780) and two giants (KIC 7374855 and KIC 9025029). Columns from left to right: M , R , $\log g$, age, and L . Red and black histograms indicate time-weighted and nonweighted PDFs. Vertical dashed lines represent the corresponding average values.

Table 2: Stellar parameters of *Kepler* planet candidate hosts.

KOI	KIC	Kepler name	T_{eff} (K)	$\log g$	[Fe/H]	M_{\star}/M_{\odot}	R_{\star}/R_{\odot}	L_{\star}/L_{\odot}	Age (Gyr)
5	8554498		5863 ± 91	4.015 ± 0.013	$+0.130 \pm 0.110$	1.23 ± 0.09	1.80 ± 0.05	3.55 ± 0.30	6.10 ± 2.44
7	11853905	Kepler-4	5820 ± 93	4.110 ± 0.010	$+0.170 \pm 0.110$	1.15 ± 0.07	1.56 ± 0.04	2.62 ± 0.22	7.11 ± 2.08
41	6521045	Kepler-100	5888 ± 91	4.130 ± 0.008	$+0.090 \pm 0.110$	1.14 ± 0.06	1.52 ± 0.04	2.59 ± 0.19	7.23 ± 1.88
75	7199397		5913 ± 88	3.758 ± 0.008	-0.110 ± 0.120	1.36 ± 0.05	2.55 ± 0.04	7.09 ± 0.54	3.51 ± 0.26
85	5866724	Kepler-65	6264 ± 101	4.232 ± 0.006	$+0.130 \pm 0.110$	1.25 ± 0.05	1.42 ± 0.02	2.81 ± 0.24	3.20 ± 0.97
108	4914423	Kepler-103	5901 ± 98	4.167 ± 0.010	$+0.100 \pm 0.120$	1.14 ± 0.06	1.46 ± 0.03	2.38 ± 0.19	6.80 ± 1.78
122	8349582	Kepler-95	5652 ± 113	4.168 ± 0.012	$+0.220 \pm 0.150$	1.07 ± 0.07	1.41 ± 0.03	1.96 ± 0.23	8.42 ± 2.15
123	5094751	Kepler-109	5992 ± 107	4.216 ± 0.014	-0.030 ± 0.130	1.09 ± 0.06	1.35 ± 0.03	2.15 ± 0.20	7.42 ± 1.52
262	11807274	Kepler-50	6271 ± 101	4.132 ± 0.008	-0.090 ± 0.120	1.23 ± 0.07	1.58 ± 0.03	3.41 ± 0.34	4.30 ± 1.49
269	7670943		6481 ± 133	4.233 ± 0.010	-0.060 ± 0.140	1.29 ± 0.06	1.43 ± 0.03	3.28 ± 0.36	2.46 ± 0.87
271	9451706	Kepler-127	6142 ± 100	4.261 ± 0.010	$+0.250 \pm 0.110$	1.22 ± 0.05	1.35 ± 0.02	2.36 ± 0.22	3.55 ± 1.15
275	10586004	Kepler-129	5802 ± 93	4.086 ± 0.009	$+0.230 \pm 0.110$	1.23 ± 0.06	1.66 ± 0.04	2.93 ± 0.21	5.33 ± 1.46
276	11133306		6013 ± 99	4.322 ± 0.010	-0.030 ± 0.120	1.08 ± 0.05	1.19 ± 0.02	1.70 ± 0.16	5.93 ± 1.41
280	4141376		6171 ± 132	4.420 ± 0.009	-0.320 ± 0.160	1.07 ± 0.06	1.05 ± 0.02	1.48 ± 0.15	2.84 ± 1.81
281	4143755		5699 ± 118	4.108 ± 0.010	-0.480 ± 0.180	0.97 ± 0.04	1.43 ± 0.03	2.09 ± 0.21	10.18 ± 0.91
285	6196457	Kepler-92	5908 ± 89	4.059 ± 0.010	$+0.150 \pm 0.110$	1.23 ± 0.07	1.71 ± 0.04	3.26 ± 0.24	5.56 ± 1.85
319	8684730		5879 ± 88	3.930 ± 0.015	$+0.080 \pm 0.110$	1.29 ± 0.12	2.04 ± 0.09	4.66 ± 0.58	5.51 ± 2.57
370	8494142	Kepler-145	6102 ± 102	4.016 ± 0.012	$+0.030 \pm 0.130$	1.25 ± 0.09	1.82 ± 0.05	4.08 ± 0.38	5.38 ± 2.07
623	12068975	Kepler-197	6129 ± 104	4.315 ± 0.014	-0.420 ± 0.140	1.00 ± 0.06	1.15 ± 0.03	1.73 ± 0.17	6.67 ± 1.91
674	7277317		4750 ± 107	3.636 ± 0.011	$+0.100 \pm 0.140$	1.10 ± 0.10	2.64 ± 0.10	3.67 ± 0.44	9.28 ± 2.57
1221	3640905	Kepler-278	4891 ± 84	3.612 ± 0.006	$+0.270 \pm 0.110$	1.27 ± 0.06	2.91 ± 0.05	4.63 ± 0.28	5.37 ± 1.12
1621	5561278		6115 ± 107	3.969 ± 0.012	-0.010 ± 0.130	1.32 ± 0.10	1.97 ± 0.07	4.83 ± 0.55	4.40 ± 1.90
1925	9955598	Kepler-409	5421 ± 93	4.496 ± 0.005	$+0.130 \pm 0.130$	0.91 ± 0.03	0.89 ± 0.01	0.64 ± 0.05	7.39 ± 1.83
2133	8219268	Kepler-91	4464 ± 80	2.933 ± 0.010	$+0.270 \pm 0.090$	1.32 ± 0.09	6.47 ± 0.19	17.56 ± 1.39	4.75 ± 1.30
2706	9697131		6313 ± 141	4.022 ± 0.013	$+0.120 \pm 0.140$	1.42 ± 0.08	1.92 ± 0.05	5.26 ± 0.66	2.79 ± 1.13
2792	11127479		5982 ± 97	4.229 ± 0.012	$+0.210 \pm 0.110$	1.15 ± 0.06	1.36 ± 0.03	2.13 ± 0.21	5.69 ± 1.68
5110	4953262		4899 ± 104	3.186 ± 0.036	-0.130 ± 0.140	1.38 ± 0.23	4.94 ± 0.44	12.58 ± 2.68	4.32 ± 2.81
5174	5524229		4971 ± 87	3.102 ± 0.035	-0.400 ± 0.130	1.41 ± 0.23	5.50 ± 0.49	16.33 ± 3.45	3.39 ± 1.88
5223	6023571		4610 ± 105	2.984 ± 0.020	$+0.180 \pm 0.120$	1.26 ± 0.17	5.96 ± 0.32	15.59 ± 2.01	6.12 ± 3.08
5281	6425377		4941 ± 148	3.107 ± 0.013	-0.010 ± 0.200	1.27 ± 0.15	5.20 ± 0.26	13.11 ± 1.59	5.23 ± 2.57
5287	6509282		4706 ± 133	2.528 ± 0.035	-0.110 ± 0.160	2.50 ± 0.42	14.20 ± 1.34	96.87 ± 22.13	0.81 ± 0.74
5322	6756369		4808 ± 114	3.228 ± 0.012	-0.190 ± 0.150	1.26 ± 0.13	4.51 ± 0.19	10.31 ± 1.13	5.04 ± 2.15
5543	8560475		4798 ± 108	2.448 ± 0.023	-0.160 ± 0.130	2.23 ± 0.43	14.67 ± 1.08	98.49 ± 23.31	1.02 ± 0.52
5578	8868481		5582 ± 90	3.774 ± 0.014	-0.040 ± 0.130	1.26 ± 0.07	2.41 ± 0.08	5.05 ± 0.51	5.25 ± 1.74
5782	10272858		4992 ± 76	3.448 ± 0.009	$+0.020 \pm 0.100$	1.34 ± 0.14	3.61 ± 0.18	7.06 ± 0.89	4.46 ± 2.09
6877	7431665		4661 ± 82	2.645 ± 0.025	-0.090 ± 0.100	1.75 ± 0.29	10.35 ± 0.64	47.06 ± 8.90	2.09 ± 1.33
7296	10214328		6624 ± 141	4.017 ± 0.014	-0.350 ± 0.140	1.36 ± 0.08	1.89 ± 0.05	6.16 ± 0.74	2.77 ± 0.61

Table 3: Stellar parameters for all the stars in this study. Only the first five rows are shown here to illustrate the format. The full table is available online.

KIC	Kepler	KOI	S/N	Kp	T_{eff} (K)	$\log g$	[Fe/H]	Mass (M_{\odot})	Radius (R_{\odot})	Luminosity (L_{\odot})	Age (Gyr)
1162746	0	0	69	11.446	4787 ± 104	2.359 ± 0.002	-0.500 ± 0.140	0.880 ± 0.005	10.26 ± 0.04	48.25 ± 1.00	11.36 ± 0.39
1163621	0	0	35	11.791	4942 ± 120	2.659 ± 0.014	$+0.020 \pm 0.150$	2.400 ± 0.223	11.98 ± 0.49	71.67 ± 8.38	0.79 ± 0.27
1294122	0	0	47	11.938	4761 ± 100	2.808 ± 0.018	-0.040 ± 0.120	1.874 ± 0.239	8.90 ± 0.48	38.76 ± 6.40	1.66 ± 1.05
1572049	0	0	66	11.571	5093 ± 128	2.679 ± 0.014	-0.220 ± 0.170	2.450 ± 0.141	11.84 ± 0.32	77.01 ± 6.12	0.66 ± 0.15
1717618	0	0	72	11.702	5019 ± 94	3.003 ± 0.016	-0.000 ± 0.120	1.910 ± 0.186	7.19 ± 0.26	27.09 ± 3.57	1.36 ± 0.46

4. RESULTS

4.1. Stellar Parameters

We applied the grid-based method, described in Section 3.1, to derive the PDFs of M , R , $\log g$, L , and age, for 3,060 stars with $\text{SNR} > 30$ spectra in the LAMOST-DR2 and DR3 Quarter 1 catalog. For each PDF, we report its mean as the result, and use standard deviation as a measure of uncertainty. Figure 3 shows examples of PDFs of M , R , $\log g$, age and L for one typical main-sequence star and two evolved stars. For comparison, we plot the time-weighted and non-weighted PDFs by using red and black solid curves, respectively. These results show that by taking into account the evolution speed effect as discussed in Section 3.1, the values of M , R , and L shift towards higher values whereas the resulting age becomes smaller. This is expected because the weights of the phases are reduced after evolving off the main sequence.

Stellar properties of planet candidate hosts are of particular interest because they are directly related to the planetary radii and masses in transit and Doppler detections. Serious uncertainties in metallicities, surface gravities, and radii, mostly based on broad-band photometry, have been found in the KIC (e.g. Verner et al. 2011; Dong et al. 2014), while high-resolution spectra are expensive for most of the *Kepler* planet hosts with $K_p < 13$ (e.g. Marcy et al. 2014). Alternatively, asteroseismology with spectroscopic inputs has been used for characterizing these planetary systems (e.g. Huber et al. 2013; Chaplin et al. 2013). There were 60 KOIs in our catalog, including 15 confirmed planet-host stars, 23 “false positives,” and 22 host candidates awaiting validation. In Table 2 we list the results for the confirmed and candidate hosts. The entire sample is available via an online catalog, and the first five rows are shown in Table 3 to illustrate the format.

Figure 4 compares the stellar parameters of the KOIs obtained in our work with those obtained in the previous studies that employed high-resolution spectroscopy. There are five stars in common with M2014, and all of them show good agreements in terms of T_{eff} , $\log g$, $[\text{Fe}/\text{H}]$, M , and R . Our derived age values were systematically higher than those in M2014, which is likely owing to the different theoretical evolution tracks used in these two studies (Y^2 in M14, and Geneva model in our study). We

also analyzed four common KOIs with Hi2012 and Hi2014, for which, the values of T_{eff} and $[\text{Fe}/\text{H}]$ obtained were systematically lower while the values of M and R were higher than the previously reported results. The stellar ages of two KOIs (KOI-269 and KOI-262) agreed within the corresponding error ranges, while the age of KOI-280 determined by us was lower. Because the main-sequence stars evolve slowly on the HR diagram compared with the post-main sequence phases, age estimation by fitting the isochrones or evolution tracks is difficult and model-dependent (see Soderblom 2010, and references therein). Our estimation based on global oscillation parameters remains meaningful because the stellar ages are further constrained by $\Delta\nu$ and ν_{max} in addition to T_{eff} , $\log g$, and $[\text{Fe}/\text{H}]$. A more detailed approach involves spectral analysis of excited oscillation modes (e.g. Silva Aguirre et al. 2015). Moreover, the field of gyrochronology, which has been developing with the help of the *Kepler* data, has made remarkable progress in refining the empirical relation between the stellar age and rotational period (e.g. García et al. 2014; Angus et al. 2015).

4.2. Comparison with Huber et al. 2014

Huber et al. (2014, hereafter, H2014) presented the stellar parameters for a large sample of *Kepler* stars observed in Quarter 1-16. Their catalog is composed of several sub-categories designated by C.1-C.14 (see their Table 1), depending on the sources of input parameters (T_{eff} , $\log g$, and $[\text{Fe}/\text{H}]$). In this sub-section we focus on common stars within the H2014 sub-categories C.1, C.4, and C.5. All of these three data sets adopted asteroseismic $\log g$, while T_{eff} and $[\text{Fe}/\text{H}]$ were obtained using various techniques (spectroscopy, photometry, and KIC). The category C.1 contains most of the “gold-standard” samples of H2014, for which high-resolution spectroscopy was used for the best possible characterization. On the other hand, stars in C.4 and C.5 had no spectroscopic temperatures or metallicities. In such cases, the authors of H2014 used a revised temperature scale by Pinsonneault et al. (2012), and their $[\text{Fe}/\text{H}]$ values were either fixed to -0.2 or obtained from KIC.

Figures 5 – 7 show the differences between the values of M , R , and L (panels a-c), as well as the atmospheric parameters T_{eff} , $\log g$, and $[\text{Fe}/\text{H}]$

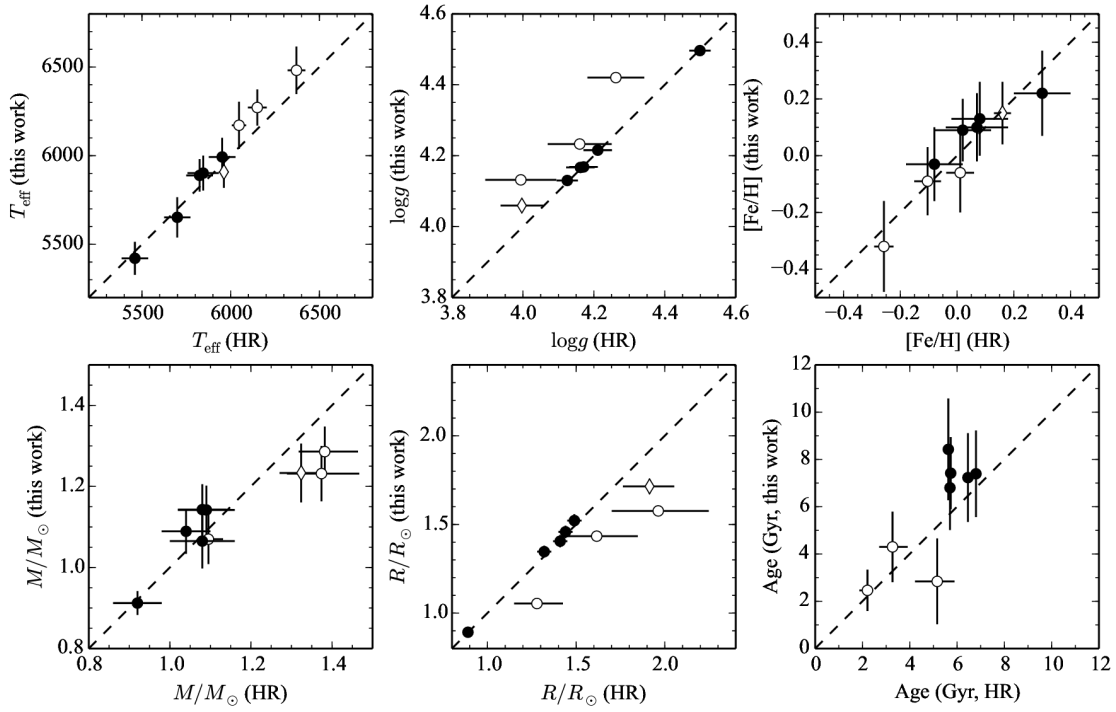


Fig. 4.— Comparison of stellar parameters for the KOIs in common with the previous studies that used high-resolution spectroscopy. Solid dots, open circles, and open diamonds represent parameters from M2014, Hi2012, and Hi2014, respectively.

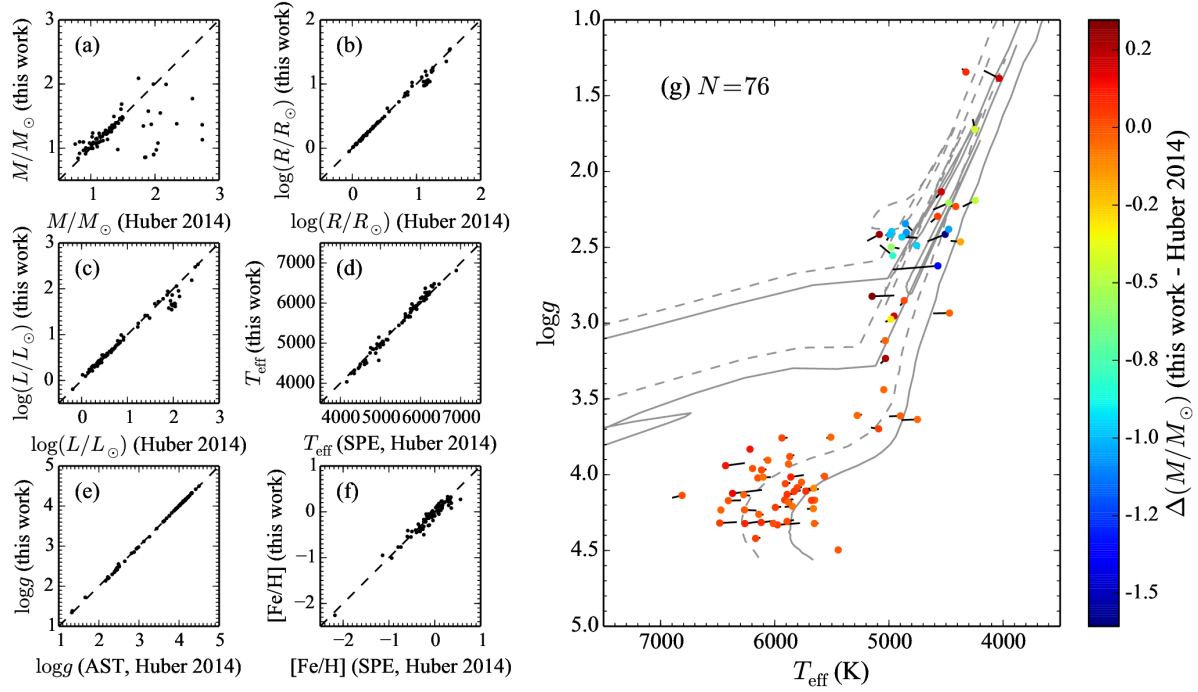


Fig. 5.— Comparisons of stellar parameters obtained in this work with those obtained from H2014 sub-category C.1 (see their Table 1). The values of T_{eff} , $\log g$, and $[\text{Fe}/\text{H}]$ in the H2014 study were obtained using spectroscopy, asteroseismology, and spectroscopy, respectively. Panel (g) shows the different positions of the sample stars on the Kiel diagram, by drawing solid lines to connect the parameters given by H2014 with those obtained in the present work. The colors are coded with ΔM (this work – H2014). A series of Geneva evolution tracks with initial masses $M_0 = 1.0, 2.0$, and $3.0 M_{\odot}$, and $[\text{Fe}/\text{H}] = 0.0$ (solid lines), and -0.5 (dashed lines) are also shown in panel (g).

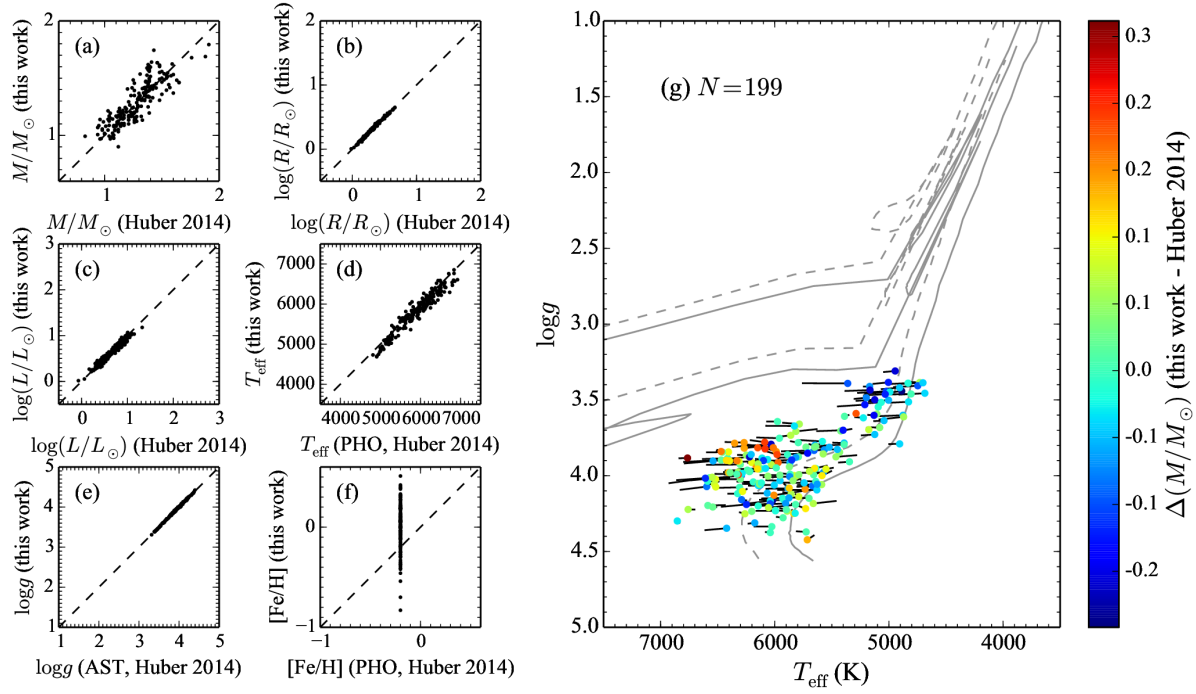


Fig. 6.— Same as Figure 5, but for stars in common with sub-category C.4 in H2014, for which the values of T_{eff} , $\log g$, and $[\text{Fe}/\text{H}]$ were obtained using photometry, asteroseismology, and photometry, respectively.

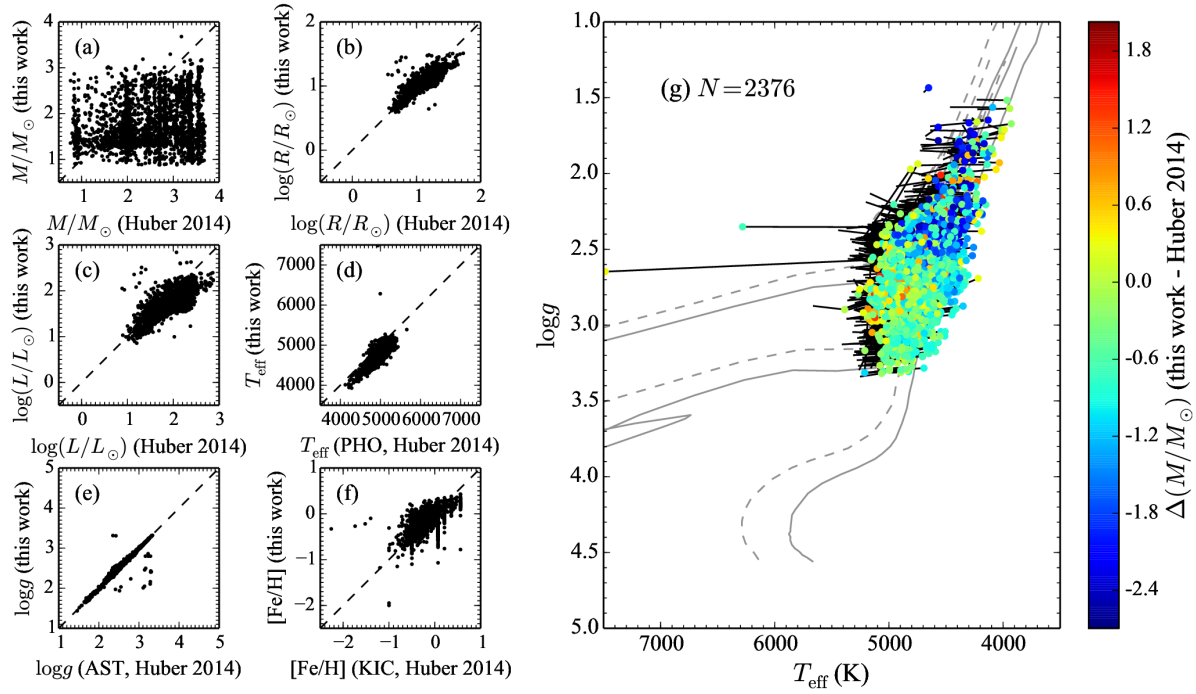


Fig. 7.— Same as Figures 5 and 6, but for stars in common with sub-category C.5 in H2014, for which the values of T_{eff} , $\log g$, and $[\text{Fe}/\text{H}]$ were obtained using photometry, asteroseismology, and the KIC, respectively.

(panels d-f) that were used as inputs. All of these reveal an excellent agreement between the values of $\log g$ in the two works, despite the fact that the values of T_{eff} and $[\text{Fe}/\text{H}]$ were taken from different sources. In each of the above figures, we also plot the differences between positions of the stars in the Kiel diagram, where the colored circles correspond to our results, and the other sides of solid lines correspond to the values from H2014. The colors are coded with ΔM (this work – H2014). Geneva evolution tracks with $M = 1.0, 2.0$, and $3.0 M_{\odot}$, and $[\text{Fe}/\text{H}] = 0.0$ (solid gray lines) and -0.5 (dashed gray lines) are also shown.

Figure 5 shows the comparison of 76 common stars including dwarfs and giants, for which both H2014 and this work used spectroscopic T_{eff} and $[\text{Fe}/\text{H}]$ as inputs for asteroseismic $\log g$ and other physical parameters. Our results are in a good agreement with the previous work, with mean differences of only 0.00 ± 0.02 , -0.02 ± 0.06 , and -0.04 ± 0.14 , for $\log g$, $\log R$, and $\log L$, respectively. All outlying points in panel (a) correspond to giants with $\log g < 3.5$, for which evolution tracks are highly degenerated in the HR diagram. We noted that our results on stellar masses for these giants are systematically lower than those from H2014. This can be explained by the bias towards higher mass in the previous studies, as discussed in Section 3.1.

Figure 6 compares the physical and spectroscopic parameters for 199 dwarfs and sub-giants in common with sub-category C.4 in H2014. Although for all of the stars in this sub-category the values of $[\text{Fe}/\text{H}]$ were fixed at -0.2 , a good agreement between the two studies was found in terms of the values of R , L , and $\log g$. On average, our T_{eff} values were 91 ± 120 K lower than the previously reported values. The mean difference between the stellar mass values was $0.01 \pm 0.10 M_{\odot}$, as shown in panel (a).

Figure 7 shows the same comparison, but for sub-category C.5 in H2014. In contrast to Figure 6, the stars in C.5 are giants, with $\log g < 3.5$. Our T_{eff} values were 226 ± 130 K lower than those reported in H2014, which subsequently significantly affected the stellar physical parameters. In terms of $\log g$, our results were in good agreement with H2014, with the mean difference of only 0.00 ± 0.08 dex. The mean differences were -0.03 ± 0.23 dex for $[\text{Fe}/\text{H}]$, -0.07 ± 0.10 for $\log R/R_{\odot}$, and

-0.23 ± 0.23 for $\log L/L_{\odot}$. Moreover, the derived stellar masses were generally lower than those in H2014, and the comparison of stellar masses in panel (a) reveals a chaotic distribution. We note that most of the masses in H2014 are in the 0.8 – $3.7 M_{\odot}$ range; however, the range was 0.9 – $3.0 M_{\odot}$ in the present study, with only a few exceptions corresponding to $M > 3.1 M_{\odot}$. These deviations can be interpreted by the facts that (1) our spectroscopic T_{eff} values obtained from low-resolution spectra were systematically lower than those reported in H2014, which were photometric T_{eff} from Sloan Digital Sky Survey *griz* filters (Pinsonneault et al. 2012); and (2) our approach correct the bias caused by different evolution speeds. Therefore, the overall distribution shifted rightward towards the tracks of less massive evolved stars on the Kiel diagram. Despite this, as $M \propto T_{\text{eff}}^{3/2}$ whereas $\log g \propto 0.5 \log T_{\text{eff}}$ according to Equations 3 and 6, and $\log g \propto \log M/R^2$ is explicitly related to ν_{max} in Equation 2, independent of metallicity. It is not surprising that a good agreement was found between the values of $\log g$ in the two studies.

Figures 5–7 show that although asteroseismology yields satisfactory $\log g$ insensitive to T_{eff} , the determination of stellar masses, and especially for giants, remains a challenge without reliable T_{eff} and $[\text{Fe}/\text{H}]$. Because the masses and radii of extra-solar planets are usually measured in terms of ratios relative to their host stars, the influence of inaccurate stellar T_{eff} and $[\text{Fe}/\text{H}]$ is inevitable. For giant stars, we estimate that an error of $+100$ K in T_{eff} results in a mass error of about $+0.20 M_{\odot}$ and a radius error of about $+0.61 R_{\odot}$ when using the asteroseismic grid-based method. In addition, an error of $+0.1$ dex in $[\text{Fe}/\text{H}]$ results in a mass error of $+0.23 M_{\odot}$ and a radius error of about $+0.74 R_{\odot}$. This in turn emphasizes the importance of spectroscopic analysis of planet-hosting giant stars, for characterizing the planetary properties. However, this effect is not significant for dwarfs.

4.3. Calibration of the LAMOST $\log g$ Values

By comparing the LAMOST $\log g$ values with asteroseismic $\log g$ values adopted in this work, we found that their difference exhibited a clear trend in the $T_{\text{eff}} - \log g$ plane, implying a possibility to establish calibration relations for $\log g$ values of LAMOST samples. To obtain reliable relation-

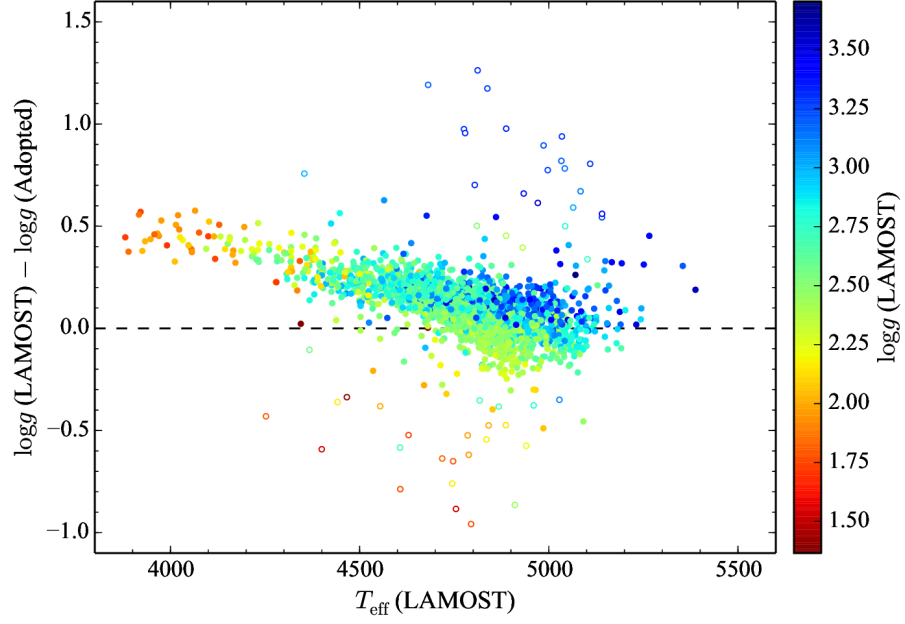


Fig. 8.— $\Delta \log g$ (LAMOST – Adopted) vs. T_{eff} for 2,094 giants. Color code correspond to the LAMOST $\log g$ values. Closed points are stars that were used in the least square fitting, while open circles represent the excluded outliers (see Text).

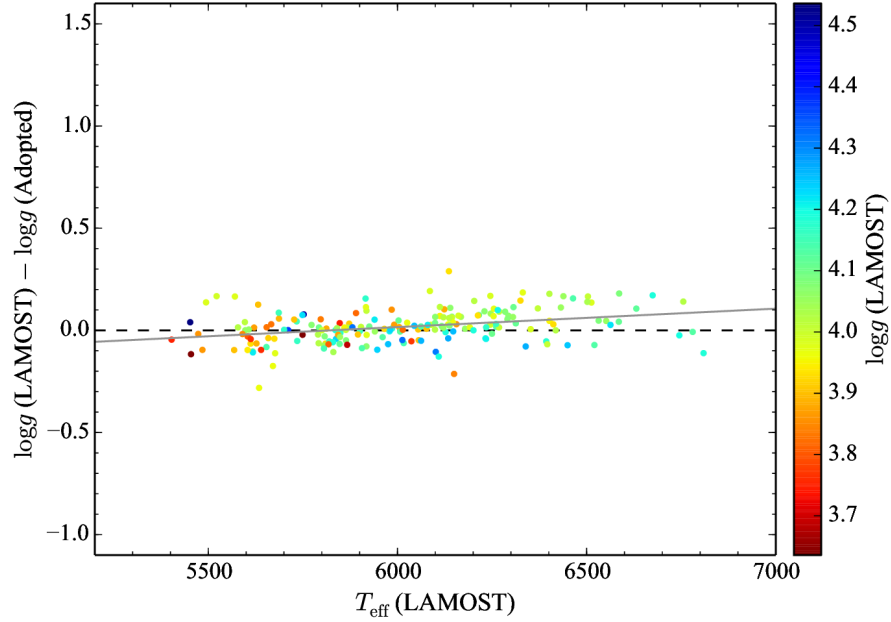


Fig. 9.— Similar to Figure 8 but for 195 dwarfs. The solid line is the best linear fit to the data points. The color code used in this figure is different from that in Figure 8.

ships, we excluded all spectra with $\text{SNR} < 50$, and adopted the atmospheric parameters based on the spectra with highest SNR, if there were multiple observations for the same star in the LAMOST DR2 and DR3 Quarter 1 catalog. This left us 2,289 samples, including 2,094 giants and 195 dwarfs.

In Figure 8 we show the differences between $\log g_{\text{(LAMOST)}}$ and $\log g_{\text{(Adopted)}}$ as a function of T_{eff} , with color coded by LAMOST $\log g$, for 2,094 giants with $T_{\text{eff}} < 5,400$ K and $\log g < 3.5$. We used a first order 2D polynomial function $f(x, y) = p_0 + p_1x + p_2y + p_3xy$ to model $\Delta \log g$, where x is T_{eff} and y is $\log g$. The coefficients $p_0 \sim p_3$ were determined by least squares fitting. After the coefficients were determined, the residuals of the fitting for all the data points were calculated. In the next step, the points with residuals falling outside $\pm 3\sigma$ were removed, and the least squares fitting was performed again. The procedure converged after two iterations, when all residuals were within $\pm 3\sigma$. There are 2,044 stars left out of 2,094 giants. This means that $\sim 2\%$ of the giants in Figure 8 are outliers that were not included in the fitting procedure. The final relation was

$$\begin{aligned} \log g_{\text{(Adopted)}} &= \log g_{\text{(LAMOST)}} \\ &- 5.716 + 1.283 \times T_3 + 1.188 \times \log g_{\text{(LAMOST)}} \\ &- 0.2882 \times T_3 \times \log g_{\text{(LAMOST)}} \end{aligned} \quad (12)$$

, where $T_3 = T_{\text{eff}}/10^3$ K is the normalized temperature from the LAMOST. The range of temperatures in which this relation is applicable is $3,800 \text{ K} \leq T_{\text{eff}} \leq 4,500 \text{ K}$ for stars with $+1.3 \leq \log g \leq 2.2$, or $3,800 \text{ K} \leq T_{\text{eff}} \leq 5,200 \text{ K}$ for stars with $+2.2 \leq \log g \leq 3.5$. In Figure 10, we show the residuals of fitting, namely $\Delta \log g_{\text{(Adopted)}}$ for giants against T_{eff} (LAMOST) within a range of 0.3 dex in each panel, with $\log g$ in the 1.7-3.5 range. The RMS values of $\log g$ in each panel were comparable, varying from 0.07 to 0.12 dex. We also calculated the RMS for these stars with T_{eff} in steps of 200 K, and obtained a 0.07-0.10 dex variation range. The overall RMS for all giants, excluding the outliers, was 0.082 dex.

Figure 9 shows the same relation for dwarfs with $T_{\text{eff}} > 5,400$ K and $\log g > 3.5$. It is seen that $\Delta \log g_{\text{(LAMOST - Adopted)}}$ has a weak dependence on T_{eff} , but no dependence on $\log g$. Therefore, we only performed a linear least squares fit,

which yielded

$$\begin{aligned} \log g_{\text{(Adopted)}} &= \log g_{\text{(LAMOST)}} \\ &+ 0.525 - 0.0902 \times T_3 \end{aligned} \quad (13)$$

, where T_3 and $\log g_{\text{(LAMOST)}}$ are the same as those in Equation 12. The applicable range is $5,400 \text{ K} \leq T_{\text{eff}} \leq 7,000 \text{ K}$, and $+3.5 \leq \log g \leq +4.5$. The RMS value was only 0.075 dex, and the residuals are plotted in Figure 10 (Right).

In Figure 11 we show the dependence of the relation on the stellar metallicity ($[\text{Fe}/\text{H}]$) as given in the LAMOST AFGK-type star parameters catalog. We separated the entire sample into four groups, corresponding to different metallicity ranges: $[\text{Fe}/\text{H}] > +0.1$; $-0.1 < [\text{Fe}/\text{H}] < +0.1$; $-0.4 < [\text{Fe}/\text{H}] < -0.1$; and $[\text{Fe}/\text{H}] < -0.4$, as shown respectively in Panels (b)-(e) of Figure 11. Both the giants and dwarfs for different metallicities ranging from -2.0 to $+0.4$ exhibited very similar trends. Although our entire sample covered a wide range of metallicity values, from -2.26 to $+0.50$, the number of stars at the metal-poor end was very small (only 10 stars with $[\text{Fe}/\text{H}] < -1.0$). Therefore, the calibration relations are applicable for stars with $-1.0 < [\text{Fe}/\text{H}] < +0.5$, and care must be taken for stars with metallicities outside this range.

4.4. Calibration of the LAMOST T_{eff} and $[\text{Fe}/\text{H}]$ Values

As shown in Section 4.3, the correction of LAMOST $\log g$ reached 0.5 dex for cool giants among our sample stars. To quantify the impact of this change on T_{eff} and $[\text{Fe}/\text{H}]$, we iteratively performed asteroseismic and spectroscopic analyses (see Section 3.2). Figures 12 and 13 show the variations in T_{eff} and $[\text{Fe}/\text{H}]$ vs. $\Delta \log g_{\text{(Adopted - LAMOST)}}$ for giants and dwarfs, respectively. It is clear that the giants in Figure can be divided into two groups. Giants with $T_{\text{eff}} > 4,500$ K exhibit clear correlations of both ΔT_{eff} and $\Delta[\text{Fe}/\text{H}]$ with $\Delta \log g$. Linear fits yielded

$$\Delta T_{\text{eff}} = 284.9 \times \Delta \log g_{\text{(Adopted-LAMOST)}} + 3.8 \quad (14)$$

and

$$\Delta[\text{Fe}/\text{H}] = 0.216 \times \Delta \log g_{\text{(Adopted-LAMOST)}} + 0.008 \quad (15)$$

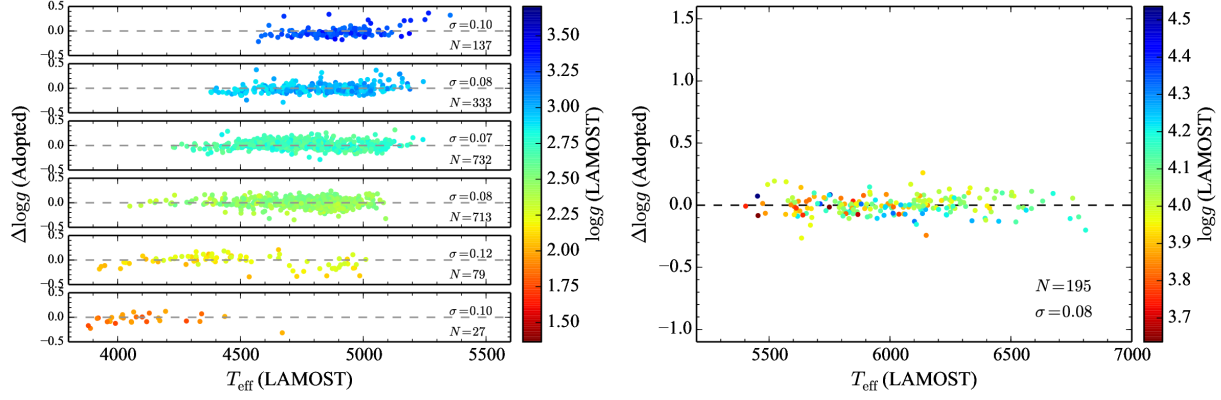


Fig. 10.— $\Delta \log g$ (Adopted) for giants (left panel) and dwarfs (right panel) used in the least squares fitting. The residuals for giants are divided into six groups of $\log g$ varying in steps of 0.3 dex, from 1.7 (bottom panel) to 3.5 (top panel). The RMS values for data in each panel are also shown.

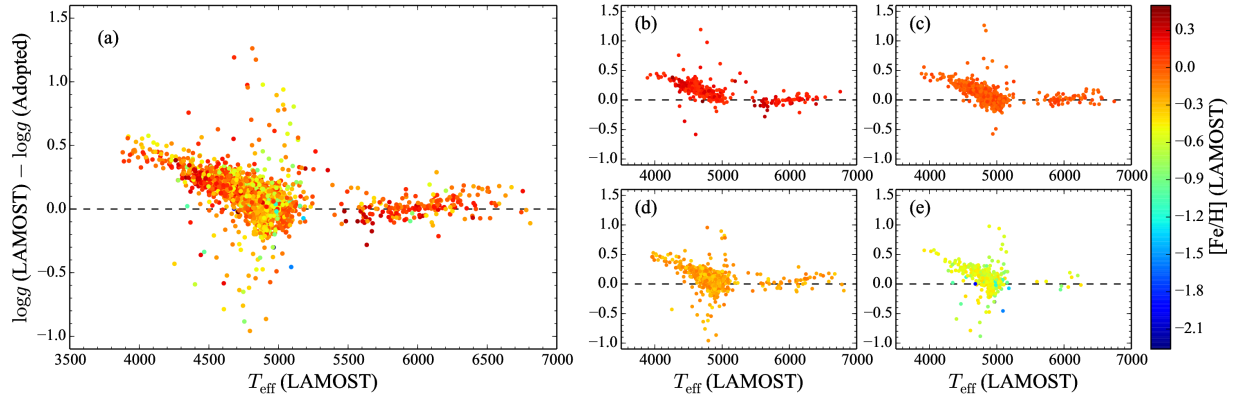


Fig. 11.— Panel (a) shows the same relation as shown in Figures 8 and 9, but with colors coded based on $[\text{Fe}/\text{H}]$. The right panels show the sub-samples falling into four metallicity ranges: (b) $[\text{Fe}/\text{H}] > +0.1$; (c) $-0.1 < [\text{Fe}/\text{H}] < +0.1$; (d) $-0.4 < [\text{Fe}/\text{H}] < -0.1$; and (e) $[\text{Fe}/\text{H}] < -0.4$. The number of stars in the four subsamples were 409, 702, 831, and 347, respectively. The right panels use the same color scale as panel (a).

, where the finally adopted equations were $T_{\text{eff}} = T_{\text{eff (LAMOST)}} + \Delta T_{\text{eff}}$, and $[\text{Fe}/\text{H}] = [\text{Fe}/\text{H}]_{\text{(LAMOST)}} + \Delta[\text{Fe}/\text{H}]$. The RMS values for the above two equations were 18.4 K and 0.026 dex, respectively. On the other hand, the ΔT_{eff} for cooler giants ($T_{\text{eff}} < 4,500$ K) exhibited no clear trends with $\Delta \log g (\text{Adopted} - \text{LAMOST})$.

Figure 13 shows that ΔT_{eff} and $\Delta[\text{Fe}/\text{H}]$ are significantly correlated with $\Delta \log g (\text{Adopted} - \text{LAMOST})$ for dwarfs. Linear fits yielded

$$\Delta T_{\text{eff}} = 292.4 \times \Delta \log g (\text{Adopted} - \text{LAMOST}) + 14.3 \quad (16)$$

and

$$\Delta[\text{Fe}/\text{H}] = 0.103 \times \Delta \log g (\text{Adopted} - \text{LAMOST}) + 0.009 \quad (17)$$

, with the RMS values of 34.6 K and 0.024 dex, respectively.

4.5. Summary

In this section, we propose empirical calibration relations for LAMOST $\log g$ in Equations 12 and 13 for giants and dwarfs, respectively. Generally speaking, the absolute values of $\log g$ corrections are much larger for giants than dwarfs, which reflects the difficulty associated with obtaining precise $\log g$ for evolved stars using low-resolution spectra. For the coolest giants in our sample, with temperatures around 4,000 K, the magnitude of corrections reached 0.5 dex. Because no systematic bias between asteroseismic $\log g$ and spectroscopic $\log g$ values has been found previously, the deviations of the LAMOST $\log g$ values from the asteroseismic ones are likely attributed to the adopted pipeline. Because such major modifications of $\log g$ would inevitably affect the determination of both T_{eff} and $[\text{Fe}/\text{H}]$, we provided the T_{eff} and $[\text{Fe}/\text{H}]$ corrections in Equations 14 – 17. Although the relations were derived for the *Kepler* targets, they are applicable to any LAMOST stars with spectroscopic parameters in the ranges given in Sections 4.3 and 4.4. The corrections of $\log g$, T_{eff} and $[\text{Fe}/\text{H}]$ should always be applied together.

Due to their high luminosity, giant stars are visible from longer distances than dwarfs and play important roles in probing the Galactic structure, kinetics, and chemical evolution. Because $g \sim MR^{-2}$, an overestimation of 0.5 dex of $\log g$ for a K4 giant with T_{eff} of 4,000 K implies that the

radius is underestimated by $0.5 \ln(10) \Delta \log g \simeq$, or 58% by assuming a fixed M . This in turn causes $\sim 115\%$ underestimation of stellar luminosity as $L \sim R^2 T_{\text{eff}}^4$. Here T_{eff} is fixed because, according to Figure 12, it nearly does not change with $\log g$. Furthermore, considering that $L = 4\pi D^2 F$, where D denotes the distance and F is the observed flux density, the luminosity distance is also underestimated by $\sim 58\%$ if the interstellar extinction is ignored. For a typical K1 giant with T_{eff} of 4,600 K and $\log g$ of 2.8, LAMOST overestimates its actual $\log g$ by ~ 0.22 dex; consequently, the values of R , L , and D will be underestimated by 25%, 50%, and 25%, respectively. However, given that T_{eff} is also reduced by ~ 56 K (according to Equation 12), the impact of increasing R on L will be offset by $\sim 5\%$. Therefore, the resulting luminosity and distance need to be increased by 45% and 22%, respectively. Another example is a red-clump giant with $T_{\text{eff}} = 4,900$ K and $\log g = 2.6$, for which the correction of $\log g$ is close to zero. Thus, previous works based on LAMOST red-clump giants (e.g. Wan et al. 2015) are nearly not affected by the systematic deviations of $\log g$.

5. CONCLUSIONS

In this paper, we consistently derived stellar parameters for a large sample of stars with the oscillation data from the *Kepler* mission, along with the T_{eff} and $[\text{Fe}/\text{H}]$ values from the LAMOST low-resolution ($R \sim 1,800$) spectra. Spanning a wide range of metallicity values ($-2.3 < [\text{Fe}/\text{H}] < +0.5$), the entire sample contained 2,831 giants and 229 dwarfs, of which 15 have been confirmed to harbor extra-solar planets and 22 were potential planet-host candidates. The stellar properties were calculated using an improved grid-based method, by considering the evolution speed effect and the post-RGB phases. The fact that T_{eff} and $[\text{Fe}/\text{H}]$ values were derived from the spectra with $\text{SNR} > 30$ and $\log g$ values were derived from the *Kepler* oscillation parameters ensure the accuracy of our results, compensating for the shortage of low-resolution spectroscopy. By comparing the asteroseismology and spectroscopic results, we found that LAMOST yielded systematically higher $\log g$ for giants, and the overestimation exhibited clear trends with T_{eff} and $\log g$. We established calibration relations for the $\log g$ of LAMOST for both giants and dwarfs. The post-

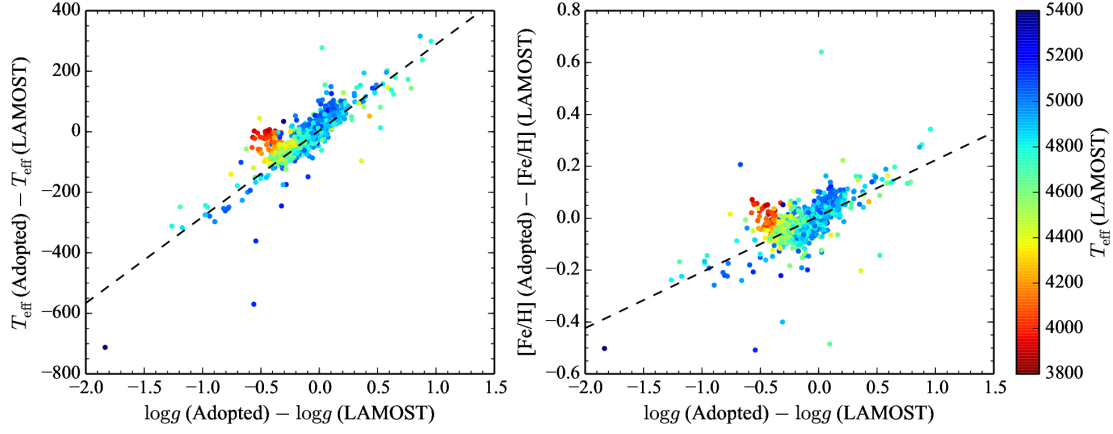


Fig. 12.— Variations in T_{eff} (left panel) and $[\text{Fe}/\text{H}]$ (right panel) vs. $\Delta \log g$ for giants, with colors coded based on T_{eff} . The dashed lines are the linear least squares fits for stars with $T_{\text{eff}} > 4,500$ K (see Text).

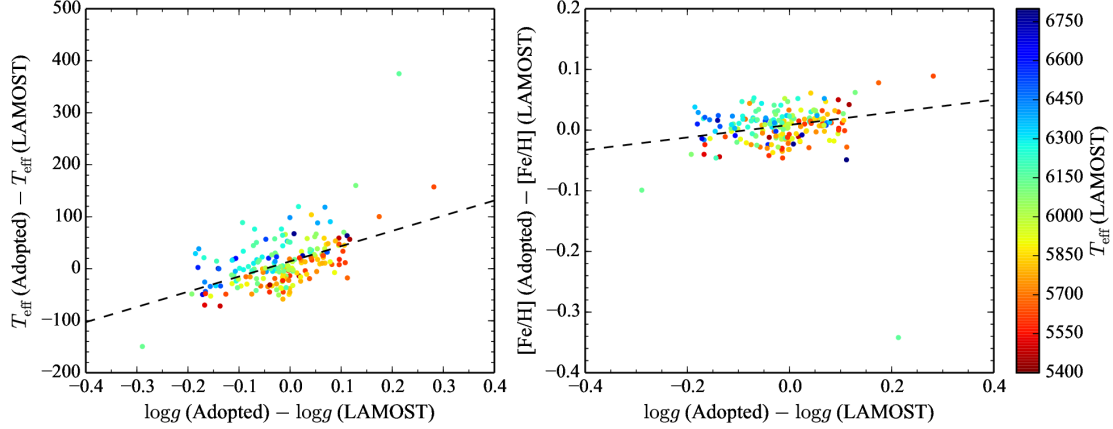


Fig. 13.— Same as Figure 12 but for dwarfs. The dashed lines are the linear least squares fits.

calibration uncertainty in $\log g$ was 0.08 dex for both giants and dwarfs, corresponding to distance errors of only 8%. The empirical relations were established for a range of stars, from mildly metal-poor ($[\text{Fe}/\text{H}] \sim -1.0$) to those with super-solar metallicity ($[\text{Fe}/\text{H}] \sim +0.4$). This range covers most of the giants and FGK dwarfs that have been observed by LAMOST. We suggest that $\log g$ of stars in this metallicity range should be corrected by using our derived relations. Meanwhile, our results regarding stellar physical parameters show that photometric T_{eff} and $[\text{Fe}/\text{H}]$ are not sufficiently accurate for obtaining reliable masses and radii for giants, even when augmented by global asteroseismic quantities. Therefore, spectroscopic studies are critical for characterization of these parameters.

This research is supported by the National Natural Science Foundation of China under grants No. 11390371 and 11403056. The Guoshoujing Telescope (the Large Sky Area Multi-Object Fiber Spectroscopic Telescope, LAMOST) is a National Major Scientific Project built by the Chinese Academy of Sciences. Funding for the project has been provided by the National Development and Reform Commission. LAMOST is operated and managed by the National Astronomical Observatories, Chinese Academy of Sciences. LW thanks Tim Bedding, William Chaplin, Saskia Hekker, Daniel Huber, Kalinge and Dennis Stello for providing the seismic data, and Tanda Li for helpful discussions.

REFERENCES

- Alexander, D. R., & Ferguson, J. W. 1994, *ApJ*, 437, 879
- Angus, R., Aigrain, S., Foreman-Mackey, D., & McQuillan, A. 2015, *MNRAS*, 450, 1787
- Basu, S., Chaplin, W. J., & Elsworth, Y. 2010, *ApJ*, 710, 1596
- Boesgaard, A. M., Rich, J. A., Levesque, E. M., & Bowler, B. P. 2011, *ApJ*, 743, 140
- Borucki, W. J., Koch, D., Basri, G., et al. 2010, *Science*, 327, 977
- Breddels, M. A., Smith, M. C., Helmi, A., et al. 2010, *A&A*, 511, A90
- Brown, T. M., Gilliland, R. L., Noyes, R. W., & Ramsey, L. W. 1991, *ApJ*, 368, 599
- Brown, T. M., Latham, D. W., Everett, M. E., & Esquerdo, G. A. 2011, *AJ*, 142, 112
- Bruntt, H., Basu, S., Smalley, B., et al. 2012, *MNRAS*, 423, 122
- Buchhave, L. A., Latham, D. W., Johansen, A., et al. 2012, *Nature*, 486, 375
- Carlin, J. L., Liu, C., Newberg, H. J., et al. 2015, *AJ*, 150, 4
- Cenarro, A. J., Peletier, R. F., Sánchez-Blázquez, P., et al. 2007, *MNRAS*, 374, 664
- Chaplin, W. J., Kjeldsen, H., Christensen-Dalsgaard, J., et al. 2011, *Science*, 332, 213
- Chaplin, W. J., Sanchis-Ojeda, R., Campante, T. L., et al. 2013, *ApJ*, 766, 101
- Chaplin, W. J., Basu, S., Huber, D., et al. 2014, *ApJS*, 210, 1
- Chen, Y. Q., Nissen, P. E., Zhao, G., Zhang, H. W., & Benoni, T. 2000, *A&AS*, 141, 491
- Chmielewski, Y. 2000, *A&A*, 353, 666
- Cui, X.-Q., Zhao, Y.-H., Chu, Y.-Q., et al. 2012, *Research in Astronomy and Astrophysics*, 12, 1197
- da Silva, L., Girardi, L., Pasquini, L., et al. 2006, *A&A*, 458, 609
- De Cat, P., Fu, J. N., Ren, A. B., et al. 2015, *ApJS*, 220, 19
- de Jager, C., Nieuwenhuijzen, H., & van der Hucht, K. A. 1988, *A&AS*, 72, 259
- Deeming, T. J. 1960, *MNRAS*, 121, 52
- Demarque, P., Guenther, D. B., Li, L. H., Mazumdar, A., & Straka, C. W. 2008, *Ap&SS*, 316, 31
- Dong, S., Zheng, Z., Zhu, Z., et al. 2014, *ApJ*, 789, L3
- Dotter, A., Chaboyer, B., Jevremović, D., et al. 2008, *ApJS*, 178, 89
- Fuhrmann, K. 1998, *A&A*, 338, 161

- Gai, N., Basu, S., Chaplin, W. J., & Elsworth, Y. 2011, *ApJ*, 730, 63
- García, R. A., Ceillier, T., Salabert, D., et al. 2014, *A&A*, 572, A34
- Hekker, S., Elsworth, Y., Mosser, B., et al. 2013, *A&A*, 556, A59
- Hekker, S., Broomhall, A.-M., Chaplin, W. J., et al. 2010, *MNRAS*, 402, 2049
- Hekker, S., Gilliland, R. L., Elsworth, Y., et al. 2011, *MNRAS*, 414, 2594
- Hirano, T., Sanchis-Ojeda, R., Takeda, Y., et al. 2012, *ApJ*, 756, 66
- . 2014, *ApJ*, 783, 9
- Huber, D., Stello, D., Bedding, T. R., et al. 2009, *Communications in Asteroseismology*, 160, 74
- Huber, D., Bedding, T. R., Stello, D., et al. 2011, *ApJ*, 743, 143
- Huber, D., Chaplin, W. J., Christensen-Dalsgaard, J., et al. 2013, *ApJ*, 767, 127
- Huber, D., Silva Aguirre, V., Matthews, J. M., et al. 2014, *ApJS*, 211, 2
- Iglesias, C. A., & Rogers, F. J. 1996, *ApJ*, 464, 943
- Johnson, J. A., Huber, D., Boyajian, T., et al. 2014, *ApJ*, 794, 15
- Kallinger, T., Mosser, B., Hekker, S., et al. 2010a, *A&A*, 522, A1
- Kallinger, T., Weiss, W. W., Barban, C., et al. 2010b, *A&A*, 509, A77
- Kjeldsen, H., & Bedding, T. R. 1995, *A&A*, 293, 87
- Kurucz, R. L. 1991, in *NATO Advanced Science Institutes (ASI) Series C*, Vol. 341, *NATO Advanced Science Institutes (ASI) Series C*, ed. L. Crivellari, I. Hubeny, & D. G. Hummer, 441
- Lee, Y. S., Beers, T. C., Sivarani, T., et al. 2008, *AJ*, 136, 2022
- Lejeune, T., & Schaerer, D. 2001, *A&A*, 366, 538
- Lind, K., Bergemann, M., & Asplund, M. 2012, *MNRAS*, 427, 50
- Liu, C., Fang, M., Wu, Y., et al. 2015, *ApJ*, 807, 4
- Luo, A.-L., Zhao, Y.-H., Zhao, G., et al. 2015, *Research in Astronomy and Astrophysics*, 15, 1095
- Marcy, G. W., Isaacson, H., Howard, A. W., et al. 2014, *ApJS*, 210, 20
- Mashonkina, L., Gehren, T., Shi, J.-R., Korn, A. J., & Grupp, F. 2011, *A&A*, 528, A87
- Mathur, S., Handberg, R., Campante, T. L., et al. 2011, *ApJ*, 733, 95
- Molenda-Żakowicz, J., Sousa, S. G., Frasca, A., et al. 2013, *MNRAS*, 434, 1422
- Mosser, B., & Appourchaux, T. 2009, *A&A*, 508, 877
- Mosser, B., Goupil, M. J., Belkacem, K., et al. 2012, *A&A*, 540, A143
- Piersanti, L., Tornambé, A., & Castellani, V. 2004, *MNRAS*, 353, 243
- Pinsonneault, M. H., An, D., Molenda-Żakowicz, J., et al. 2012, *ApJS*, 199, 30
- Prugniel, P., & Soubiran, C. 2001, *A&A*, 369, 1048
- Reddy, B. E., Tomkin, J., Lambert, D. L., & Alende Prieto, C. 2003, *MNRAS*, 340, 304
- Reimers, D. 1975, *Memoires of the Societe Royale des Sciences de Liege*, 8, 369
- Ren, J.-J., Liu, X.-W., Xiang, M.-S., et al. 2016, *Research in Astronomy and Astrophysics*, 16, 009
- Sánchez-Blázquez, P., Peletier, R. F., Jiménez-Vicente, J., et al. 2006, *MNRAS*, 371, 703
- Silva Aguirre, V., Davies, G. R., Basu, S., et al. 2015, *MNRAS*, 452, 2127
- Soderblom, D. R. 2010, *ARA&A*, 48, 581
- Steinmetz, M., Zwitter, T., Siebert, A., et al. 2006, *AJ*, 132, 1645

- Stello, D., Huber, D., Bedding, T. R., et al. 2013, *ApJ*, 765, L41
- Takeda, Y., & Tajitsu, A. 2015, *MNRAS*, 450, 397
- Thygesen, A. O., Frandsen, S., Bruntt, H., et al. 2012, *A&A*, 543, A160
- Ulrich, R. K. 1986, *ApJ*, 306, L37
- van Leeuwen, F. 2007, *A&A*, 474, 653
- Verner, G. A., Chaplin, W. J., Basu, S., et al. 2011, *ApJ*, 738, L28
- Vogt, S. S., Allen, S. L., Bigelow, B. C., et al. 1994, in *Society of Photo-Optical Instrumentation Engineers (SPIE) Conference Series*, Vol. 2198, *Instrumentation in Astronomy VIII*, ed. D. L. Crawford & E. R. Craine, 362
- Wan, J.-C., Liu, C., Deng, L.-C., et al. 2015, *Research in Astronomy and Astrophysics*, 15, 1166
- Wang, L., Liu, Y., Zhao, G., & Sato, B. 2011, *PASJ*, 63, 1035
- Wu, Y., Du, B., Luo, A., Zhao, Y., & Yuan, H. 2014, in *IAU Symposium*, Vol. 306, *Statistical Challenges in 21st Century Cosmology*, ed. A. Heavens, J.-L. Starck, & A. Krone-Martins, 340–342
- Wu, Y., Luo, A.-L., Li, H.-N., et al. 2011, *Research in Astronomy and Astrophysics*, 11, 924
- Xiang, M. S., Liu, X. W., Yuan, H. B., et al. 2015, *MNRAS*, 448, 822
- Xue, X.-X., Ma, Z., Rix, H.-W., et al. 2014, *ApJ*, 784, 170
- Yanny, B., Rockosi, C., Newberg, H. J., et al. 2009, *AJ*, 137, 4377
- Zwitter, T., Castelli, F., & Munari, U. 2004, *A&A*, 417, 1055
- Zwitter, T., Siebert, A., Munari, U., et al. 2008, *AJ*, 136, 421